COBEM 2021 26th International Congress of Mechanical Engineering
November 22-26, 2021, Virtual Congress, Brazil
ABCM Associação Brasileira de Engenharia e Ciências Mecânicas

COBEM-2021-1373
HIGH-ORDER CONSERVATIVE INTERPOLATION FOR UNSTEADY AERODYNAMICS APPLICATIONS

Renan Santos
Instituto Tecnológico de Aeronáutica, DCTA/ITA, São Jose dos Campos, SP, 12228-900, Brazil
renanufabc@gmail.com

João Luiz F. Azevedo
Instituto de Aeronáutica e Espaço, DCTA/IAE/ALA, São Jose dos Campos, SP, 12228-904, Brazil
joaoluiz.azevedo@gmail.com

Abstract. *The capability of handling unsteady flow over complex geometries with efficiency and high-order accuracy is quite often desirable for the aerospace industry. Recent research on high-order overset flux reconstruction methods have shown successful results over moving boundary problems without the need of remeshing. The ability of accurately handling such type of requirements is very important, for instance, when addressing rotary wing flows and similar problems. In the present study, a high-order flux reconstruction solver is implemented coupled with a high-order conservative interpolation approach and a kd-tree algorithm over the mesh nodes for data communication in the overset regions. The flow is modelled by the 2-D Euler Equations discretized in space with a spectral difference method, a Roe approximate Riemann solver with Harten's entropy correction for the flux reconstruction over the cell faces, and an explicit strong stability-preserving Runge-Kutta for time discretization. In the overset grid scenarios, two grids are generated: a background Cartesian mesh including all the fluid box domain and a near-body quadrilateral mesh. In order to determine which cell of the donor grid embeds a specific node in the receiver grid, both mesh nodes are implemented with a tree data structure expecting the logarithmic time complexity of O(k.logN) in the geometry search, where k is the order of flux points over the boundary interfaces of the receiver mesh and N the order of nodes in the donor grid. Furthermore, the solution is interpolated from the donor cell to the receiver grid point based on the donor cell polynomial expansion at the solution points and, then, imposed in a weak manner as a boundary condition to exactly reconstruct the flux with the approximate Riemann solver, as for any other interior face. The implementation is tested for different validation problems from the 5th International Workshop on High-Order CFD Methods (HiOCFD5). Additionally, accuracy and convergence studies are being performed on both single and overset grid approaches and compared to results in the literature.*

Keywords: *Overset grid, High-order methods, Unsteady aerodynamics, Computational fluid dynamics*

1 INTRODUCTION

Unsteady aerodynamics are present in several applications in the aerospace industry such as rotary wing flows, fluid structure interactions and flight control. The majority of these unsteady flows are dominated by vortices, which in order to be accurately represented at an acceptable cost and robustness, efficient high-order methods were developed in the past years (Wang, 2002; Wang and Liu, 2002; Liu *et al.*, 2006; Wang *et al.*, 2007; May and Jameson, 2006; van den Abeele *et al.*, 2007; van den Abeele, 2009; Moreira, 2016). Moreover, recent studies on high-order methods considering curved geometries have demonstrated the necessity of a suitable representation of the physical boundaries to achieve not only convergency but also the desirable phenomena of the application, (Aguiar, 2018). In order to fulfill the high-order accuracy requirements for complex geometries both the solver and the approximation of the geometry must then be high-order.

For instance, the flow around a helicopter blade or a flexible wing often require the simulation of moving boundaries. In a single mesh approach undesirable costs can emerge once at each boundary movement a remeshing procedure have to be computed. Therefore, as overset meshes can isolate the boundary in a near-body mesh that co-moves with the object while the rest of the fluid domain stays static in a background grid, no remeshing is needed, however data must be communicated between both meshes. In order to achieve the coupling, a donor-receiver relationship must be established so that the flow solution can be interpolated in the overset region. The first step is represented as a geometric search problem, which maps the outer boundary of the near-body mesh to the background and the second step requires that the solution at each time iteration is interpolated from the background to the near-body grid and vice-versa. Additionally, a cell-cutting procedure is needed to identify which cells at the background mesh are completely overlapped by the object or by the near-body mesh tagging them as hole cells, where the solver computation is not necessary. Recent works proposed different techniques for these steps and highlighted the main difficulties (Galbraith, 2013; Crabill *et al.*, 2016; Duan and

Wang, 2017, 2019, 2020).

The present work proposes an approach to handle overset high-order unstructured grids using a high-order Spectral Differences method for space discretization and an explicit Strong-Stability Preserving Runge-Kutta for time integration. For the overset coupling, a kd-tree algorithm is used as the geometric searching method due to its well established logarithmic time complexity (Bentley (1975); Skrodzki (2019)) and for the interpolation the face-based approach discussed in Duan and Wang (2017).

The sections of this paper are organized as follows. Section 2 describes the governing equations used in the present work. Section 3 reviews the Spectral Differences method and polynomial representation for high-order meshes. Section 4 contains all the overset grid treatment including the geometric search procedure and conservative high-order interpolation. Section 5 shows the results comparing single and overset grid test cases. Finally, conclusions and future extensions of the present project are discussed in Section 6.

2 EULER EQUATIONS

The flow simulations presented in this project consider the 2D Euler Equations to model the conservative properties of the fluid in time. The conservation laws represented by the Euler Equations combined with the equation of state for perfect gases form the proper equations system to describe compressible and inviscid flows and can be written as

$$\frac{\partial Q}{\partial t} + \frac{\partial F}{\partial x} + \frac{\partial G}{\partial y} = 0 \, . \tag{1}$$

where Q is the vector of conserved variables, F and G the inviscid flux vectors given by

$$Q = \left\{ \begin{array}{c} \rho \\ \rho u \\ \rho v \\ E \end{array} \right\} , \qquad F = \left\{ \begin{array}{c} \rho u \\ \rho u^2 + p \\ \rho uv \\ u(E+p) \end{array} \right\} , \qquad G = \left\{ \begin{array}{c} \rho v \\ \rho uv \\ \rho v^2 + p \\ v(E+p) \end{array} \right\} . \tag{2}$$

The ρ is the density, p is the pressure, E is the total energy, u and v the velocity components in x and y direction, respectively. The pressure is defined by the equation of state for perfect gases as

$$p = (\gamma - 1) \left[E - \frac{1}{2} \rho (u^2 + v^2) \right] , \tag{3}$$

where the isentropic coefficient of air (γ) is 1.4.

3 NUMERICAL DISCRETIZATION

This section is a brief description of the space and time discretization approaches used in the present work. A more elaborated overview can be found in Liu *et al.* (2006), Wang *et al.* (2007), May and Jameson (2006), van den Abeele (2009), and Moreira (2016).

The space discretization procedure of the presented governing equations throughout all simulations in this work was made by a high-order Spectral Differences method (SD) due Wang *et al.* (2007). The formulation can properly handle quadrilateral cells given an arbitrary solution accuracy order in an efficient manner by transforming each cell from its physical x, y domain into a particular computational ξ, η domain over the interval $[-1, 1]$ allowing high-order solution interpolation as presented in Wang *et al.* (2007) and May and Jameson (2006). The governing equations in the physical space are then transformed into the computational space, and are rewritten as

$$\frac{\partial \tilde{Q}}{\partial t} + \frac{\partial \tilde{F}}{\partial \xi} + \frac{\partial \tilde{G}}{\partial \eta} = 0 \, , \tag{4}$$

or in its divergence form as

$$\frac{\partial \tilde{Q}}{\partial t} + \nabla_{\xi,\eta} \bullet \tilde{\mathbf{F}} = 0 \, . \tag{5}$$

where the conservative variables in the computational space are defined by $\tilde{Q} = |J| \, Q$, the flux vector $\tilde{\mathbf{F}} = |J|[J]^{-1}\mathbf{F}$, and J the Jacobian matrix of the coordinate transformation given by

$$J = \left(\begin{array}{cc} x_\xi & x_\eta \\ y_\xi & y_\eta \end{array} \right) . \tag{6}$$

This transformation also permits a high-order quadrilateral representation for curved boundaries by considering N equally spaced nodes in the quadrilateral computational space to construct the space transformation Jacobian matrix. The space projection from the physical to the computational space for each quadrilateral is then computed by

$$x(\xi,\eta) = \sum_{m=1}^{(N+1)^2} L_m^{N+1}(\xi) L_m^{N+1}(\eta) x_m \qquad y(\xi,\eta) = \sum_{m=1}^{(N+1)^2} L_m^{N+1}(\xi) L_m^{N+1}(\eta) y_m \tag{7}$$

where m iterates through all nodes of a N-th order quadrilateral and L^{N+1} is the (N+1)-th order Lagrange polynomial basis, i.e,

$$L_m^{N+1}(\xi) = \prod_{k=1,k\neq m}^{N+1} \frac{(\xi - \xi_k)}{(\xi_m - \xi_k)} \, . \tag{8}$$

Furthermore, two sets of intra-cell grid points are allocated, named as solution points (SP) and flux points (FP). The former set storages the nodal values of the conserved variables Q and are located at the Gauss-Legendre quadrature points. The latter storages the nodal values of the flux vectors F and G splitted in two flux point groups located at a combination of the Gauss-Legendre and Gauss-Legendre-Lobatto roots to achieve a stable method according to van den Abeele (2009). Figure 1 illustrates the cell domain transformation as well as the intra cell grid disposal.

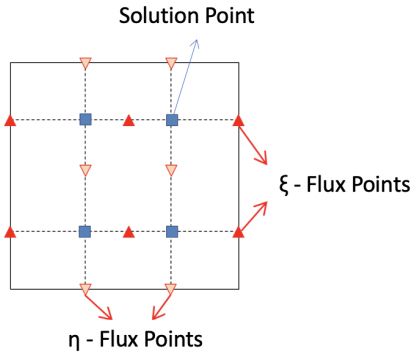

Figure 1. Quadrilateral in computational space for second-order Spectral Differences, $p = 1$.

The conserved solution can then be constructed at any target position within the cell computational domain by a nodal interpolation using a Lagrange polynomial basis as

$$Q_i(\xi,\eta) = \sum_{j=1}^{N_p} L_j^p(\xi) L_j^p(\eta) Q_{i,j} \, . \tag{9}$$

where i is the i-th cell index, j the j-th solution point at the i-th cell, N_p the number of basis functions required to construct a p order polynomial interpolation, and L^p is the p-th order Lagrange polynomial basis.

The solution vector at the flux points is computed through the Eq. 9 and since its value is only contiguous within the cell domain, solution discontinuities at the cell interfaces can emerge. Hence, the normal flux at the edges flux points is then reconstructed through a Riemann solver which for all simulations in this work a Roe scheme was used. Since only the normal component can affect the conservation properties through the cells interface, the tangential part of the flux is averaged. The basic formulation for the flux reconstruction can be written as

$$\tilde{F}_n = \frac{1}{2}\{(F_L + F_R) \bullet \mathbf{n} + |A|(Q_L - Q_R)\} \, . \tag{10}$$

where L and R subscripts represent respectively the left and right cells of an edge and $|A|$ is a representation of the Jacobian matrix of the flux vector which for Roe scheme is assumed to be constant between the two cells at the interface. Details on the Roe Riemann solver can be found in Roe (1981).

Moreover, after all the flux vectors have been computed - by the Riemann solver at the edges and by Eq. 2 at the other flux points - each component of the reconstructed flux divergence is then interpolated similarly as in Eq. 9, however, considering the respective flux point group as

$$\nabla \bullet \mathbf{F}_i(\xi,\eta) = \sum_{j=1}^{N_{p+1}} \nabla M(\xi,\eta) \bullet \mathbf{F}_{i,j} \, . \tag{11}$$

where j is the j-th flux point of the i-th cell, the superscript $p+1$ indicates that for each flux component the interpolation is one order higher than the solution interpolation at Eq. 9 providing the same p-th polynomial order after the divergence computation, $\mathbf{F}$ is the flux vector and M represents the Lagrange polynomial basis.

At the end, the solution is computed by the discretized governing equation written as

$$\frac{\partial Q_{i,j}}{\partial t} + \sum_{k=1}^{N_{p+1}} \nabla M(\xi_j, \eta_j) \bullet \mathbf{F}_{i,k} = 0 \,. \tag{12}$$

The time integration is calculated by an explicit Strongly-Stability Preserving (SSP) Runge-Kutta scheme described in Gottlieb *et al.* (2018) and Ruuth *et al.* (2002). Additionally, curved boundary treatments based on NURBS are considered in the mesh generation following the work described in Aguiar (2018).

4 OVERSET GRIDS

For overset grids simulations, two quadrilateral meshes are generated. A Cartesian grid for the overall fluid domain and a smooth near-body grid. This configuration provides a considerable processing cost reduction during the simulation in particular for moving boundaries cases, once only the near-body grid have to be remeshed as discussed in Duan and Wang (2017), Duan and Wang (2019) and Crabill *et al.* (2016). In order to solve the numerical iterations, data must be shared within the overset region so that it preserves the conservative property and high-order accuracy in both the donor and the receiver meshes. Two steps are important to formulate the data communication: a geometric search to establish the donor-receiver relationship and a conservative high-order approach for the data interpolation.

4.1 Geometric search

The definition of a donor-receiver relationship is necessary to communicate data from cells in the background mesh to nodes over the external boundary in the near-body mesh and to cut off cells in the background mesh that is completely overlapped by the near-body mesh domain. In order to simplify both applications, two types of cells are defined, respectively: fringes and holes. Fringes will receive and communicate data while holes will be passed during the iterations and no equation will be solved for them.

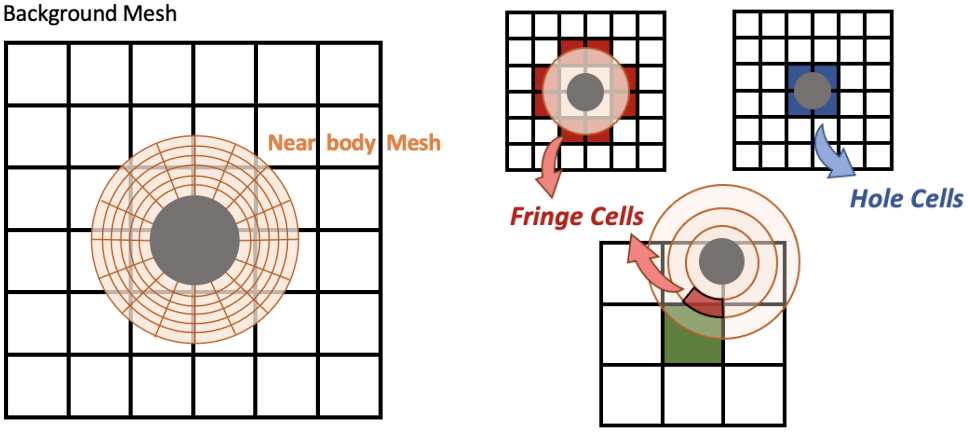

(a) Overset meshes setup: background mesh in black and near-body mesh in orange.

(b) Definitions of cell types: fringes (red) are used to interpolate solution while holes (blue) bypass the solver. The green cell is the same fringe cell in red as before, but changed to emphasize near-body fringes.

Figure 2. Overset grid setup and cell type definitions for a illustrative cylinder example.

The geometric search problem applied to the context of overset grids aims to define an efficient manner of finding which cell in the donor mesh embeds a specific node in the receiver mesh. In the present project, a kdtree algorithm described in Bentley (1975) is used for this purpose requiring a tree data structure for the node vectors in both meshes. A tree representation is well suited for this application due to its logarithmic time complexity by splitting the domain by half in each search step according to Skrodzki (2019). Figure 4 illustrates the tree structure in the fluid domain.

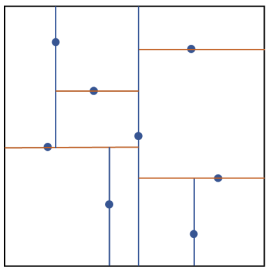

Figure 3. Kd-tree geometrical view for a given set of points.

At the end of the search process starting at a specific node from the receiver mesh, the nearest node at the donor is found and an additional step is necessary to determine which cell that owns the nearest node in fact embeds the donor node. For each cell candidate, a loop throughout its edges is done checking whether the receiver node is inside the candidate by validating the sign of the cross product between the edge and the target node as it can be seen in Fig. 4(b).

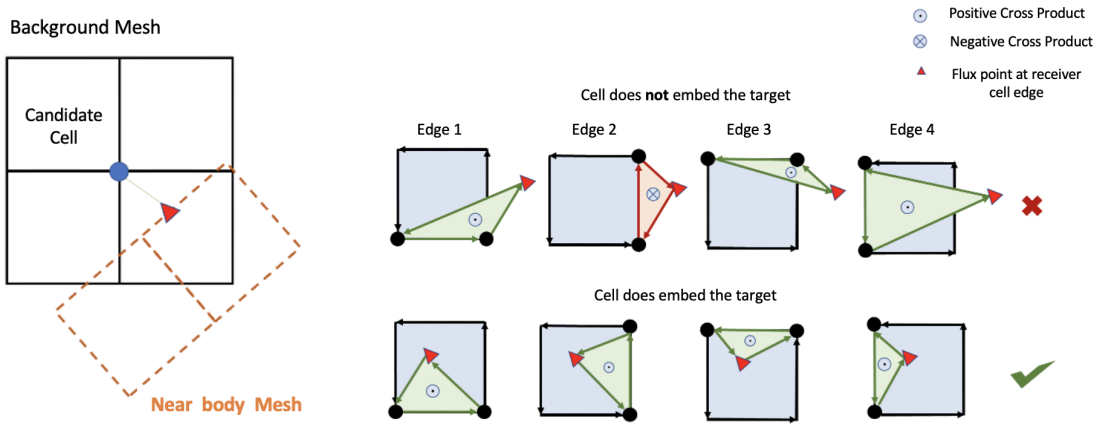

(a) Donor-receiver neighborhood in the physical space.

(b) Procedure of finding which cell of the nearest node embeds the target node.

Figure 4. Donor cell searching procedure given the target node (red triangle) and the nearest donor node (blue circle).

If all the signs are positive respecting the edges' node order, the cell candidate is embedding the receiver node and a fringe flag is attributed to this cell. The fringe cells are determined for the background mesh by applying this search process for each flux point in the ghost cells at the external boundary of the near-body mesh. For the hole cells, a random node in the near-body grid is then selected until its donor cell output in the background satisfy the conditions of not being a fringe and being completely overlapped by the near-body mesh. This cell is flagged as a hole cell and it is used as input for a breadth-first search algorithm which propagates the hole flag until all interior cells within the fringe closed circuit are visited. At last, new ghost cells are created at the fringe-hole interfaces in order to correct the flux normal to its edges by communicating data from the near-body mesh. The same donor-receiver relationship procedure is done to determine which cells at the near-body mesh embeds all flux points in these ghosts as well.

4.2 Conservative high-order interpolation

After the link between the meshes has been established, the data communication is imposed through a face-based approach which uses the donor solution points to interpolate the conservative variables to the flux points located at the fringe cells ghosts. Then the interpolated solution is used as a weak boundary condition and due to its similar discontinuities at the cell and ghost interfaces, the same Riemann solver is used to reconstruct the flux. Therefore, all the data communication is restricted to the fringe cells' ghosts.

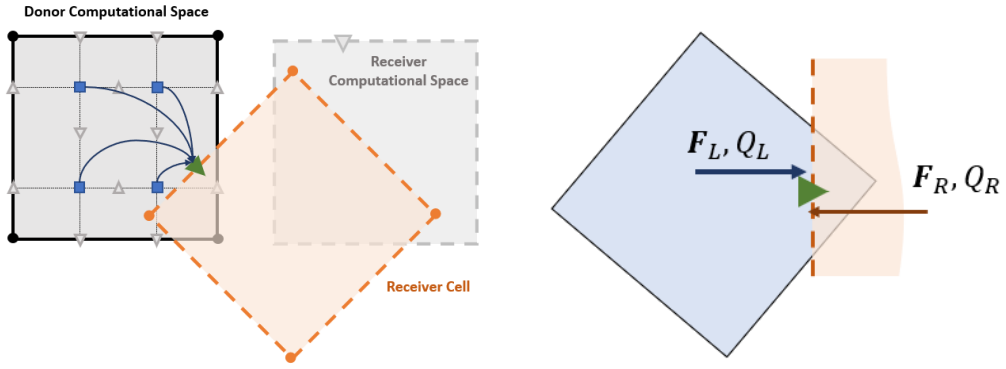

(a) Donor solution points (blue squares) interpolation to the receiver ghost cell at a target flux point.

(b) Flux reconstruction procedure at a ghost cell flux point in the receiver computational space.

Figure 5. Data communication steps including the spaces transformations (left) and the imposition of the interpolated solution as a weak boundary condition using flux reconstruction (right).

For each ghost cell tagged as an overset boundary type, a loop through its flux points is done. For each of these flux points, the physical target coordinates can be determined through the transformation defined by its neighbor cell (receiver) using the Eq. 7. Furthermore, the same Eq. 7 can be used to transform the receiver point from the physical to the donor computational space, however, a non-linear system of equations has to be resolved, which for the present work, a Newton-Raphson is used. Once the receiver flux point is properly projected into the donor computational space, the solution is then interpolated through the Eq. 9 preserving the same high-order polynomial representation used by the Spectral Differences method. Additionally, for high-order meshes the Jacobian of the transformation is not constant within the cell domain, but a function of the target ξ, η coordinates and also has to be computed in order to project the solution back to the physical space. The receiver coordinate transformation is then used to obtain the solution at the ghost cell flux point in the receiver computational domain where the Riemann solver is used to reconstruct the flux by Eq. 10. Figure 5 illustrates the interpolation procedure.

5 RESULTS

The results are divided in two test cases: Ringleb flow and inviscid cylinder flow. The former is intended to validate the high-order solver capabilities implemented in the present work and the latter as a comparative test case between the single mesh and overset mesh results. An important notation is used throughout the results section to notify the solver accuracy and mesh orders. For instance, a P2Q2 mesh considers a three-point interpolation - a parabola, thus the P2 - to achieve a third order Spectral Differences with a second order quadrilateral mesh (Q2).

5.1 Ringleb test case

The Ringleb flow is a common candidate to state the level of accuracy in high-order solvers due to its analytical solution for the Euler Equations derived from a hodograph transformation (Shapiro (1953)). Another interesting property of the Ringleb flow is that the transition from supersonic to subsonic region does not generate a shock, then no limiter is needed for this test. The analytical solution is used as initial condition and only depends on two parameters: the velocity magnitude U and the stream function interval $[k_{min}, k_{max}]$. The results obtained in this section considered $U = 0.5$, $k_{min} = 0.7$ and $k_{max} = 1.5$. The boundary conditions are imposed with a subsonic inlet at the top, a subsonic outlet at the bottom and the exact analytical solution at the inner (left) and outer (right) walls.

Figure 6(a) shows the P3Q4 mesh, forth-order mesh and solver, with 12 cells based on the validation test case of the International Workshop on High-Order Methods in CFD (Wang *et al.* (2015)). The Mach analytical field are shown in Fig. 6(b) and can be compared with the numerical Mach field in 6(c) after 1E+5 iterations. The residue history achieved machine precision around the 3E+4 iteration as it can be seen in Fig. 7.

5.2 Cylinder test case

A subsonic inviscid flow over a cylinder is considered to compare the single and overset mesh results. The simulation is setup with a free-stream Mach number of 0.2 in order to observe a double symmetry at the horizontal and vertical axis for the Mach field solution when solving the Euler equations. The mesh domain is given by 100 cylinder radius with the overall initial condition of $Mach = 0.2$, $\rho = 1$ and $p = \frac{1}{\gamma}$ assuming $\gamma = 1.4$ for the air. The boundary conditions imposed is a subsonic/supersonic inlet - depending on the normal face velocity - forcing the free-stream Mach at the entrance, a outlet at the exit forcing $p = \frac{1}{\gamma}$ for subsonic and internal solution extrapolation for supersonic, and a non-slip

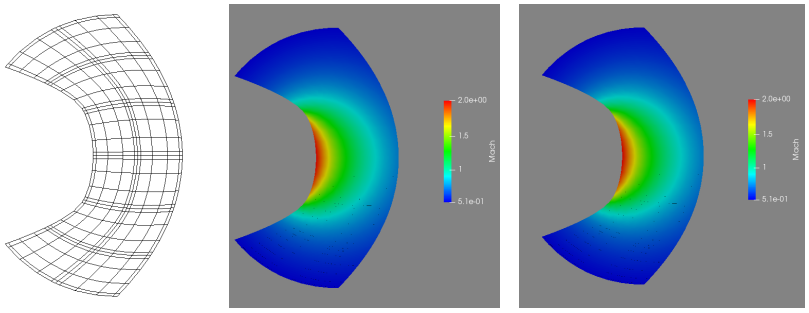

(a) (b) (c)

Figure 6. Ringleb Mach solutions: analytical (left) and numerical P3Q4 (right) after 100,000 iterations.

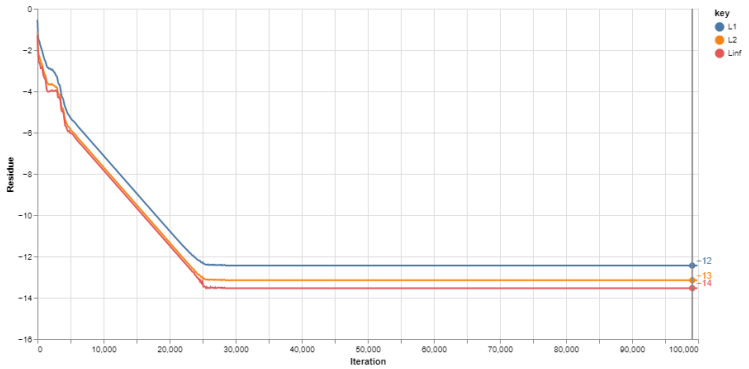

Figure 7. Ringleb residues: L_1 (blue), L_2 (orange) and L_∞ (red).

wall at the cylinder. For the overset case, an additional boundary is imposed to communicate the solution from both meshes at all overset ghost cells at each time iteration in order to reconstruct the flux in the Riemann solver step. The meshes generated for these tests considered a 20x32 mesh for P1Q1 and P4Q4 single mesh cases and a 64x64 P1Q1 for the overset. Figures 8, 9, and 10 shows the meshes. The reason for this local refinement in the overset mesh is due to difficulties in edge cases where the fringe cells are only partially enveloped by a donor cell and since the neighbor cell is deactivated (hole) the solution does not converge. This issue was critical for high-order mesh and no stable results were obtained so far for high-order overset grids. Another difficulty presented in the simulations is the sensibility in the refinement order between the cells at the outer near-body mesh and the background mesh fringes. When the background mesh refinement is too closed or higher comparing to the outer near-body, the fringe cells closed-circuit is not formed and the Breadth-First-Search starts to tag fluid cells as holes.

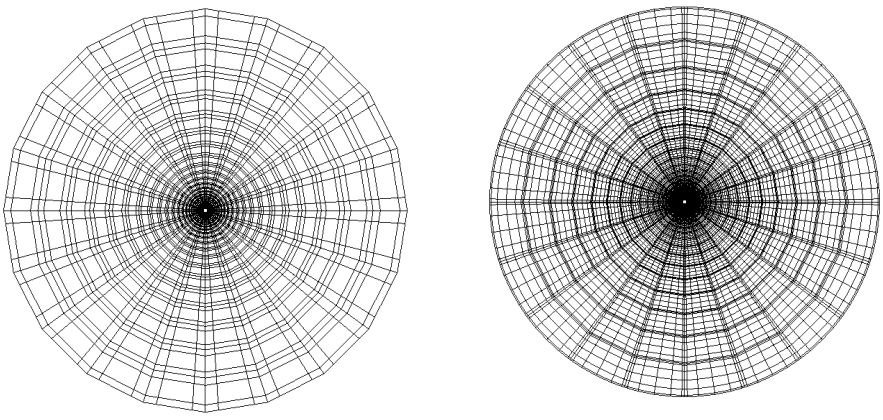

(a) Cylinder single mesh P1Q1. (b) Cylinder single mesh P4Q4.

Figure 8. Cylinder single meshes with 1:100 cylinder radius ratio.

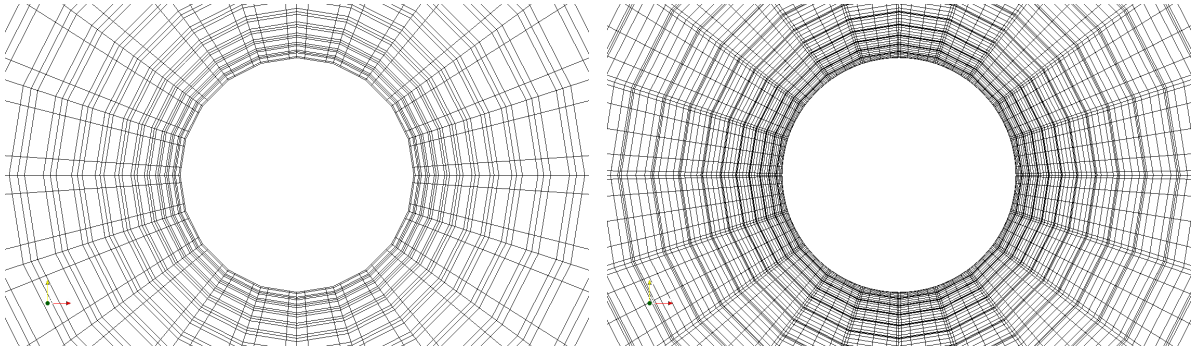

(a) Cylinder single mesh P1Q1 close-up. (b) Cylinder single mesh P4Q4 close-up.

Figure 9. Cylinder single mesh body close-up showing the curved representation for a high-order mesh.

The future extensions intend to work on this problems to improve the robustness of the proposal. However, converged results could be achieved by adjusting the mesh refinement for the P1Q1 mesh. 10. Figure 11(a) shows the background fringe cells circuit in red and the background hole cells in blue. Furthermore, Fig. 11(b) shows the fringe cells at the near-body mesh that are used to interpolate the solution to the background mesh edges that lie between fringes and holes.

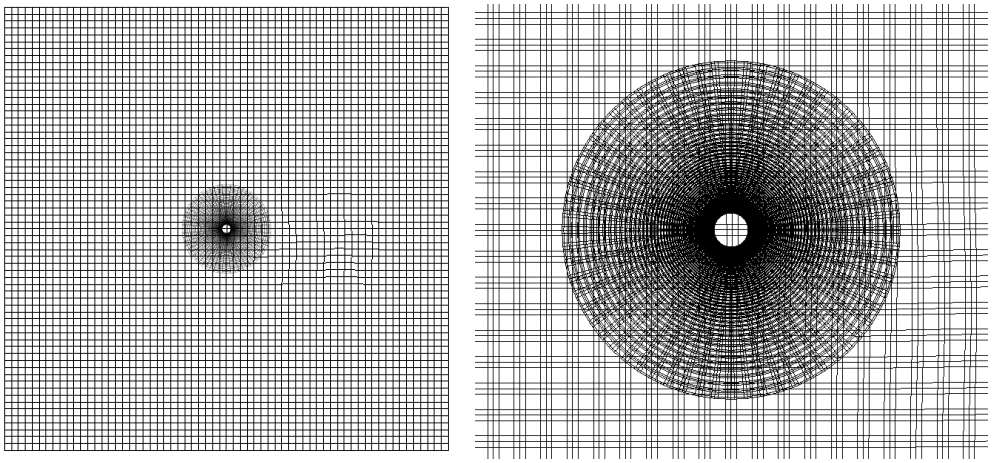

(a) Cylinder overset mesh P1Q1: a Cartesian background mesh and a near-body mesh over the cylinder. (b) Cylinder overset mesh close-up P1Q1.

Figure 10. Cylinder overset mesh overall and close-up views.

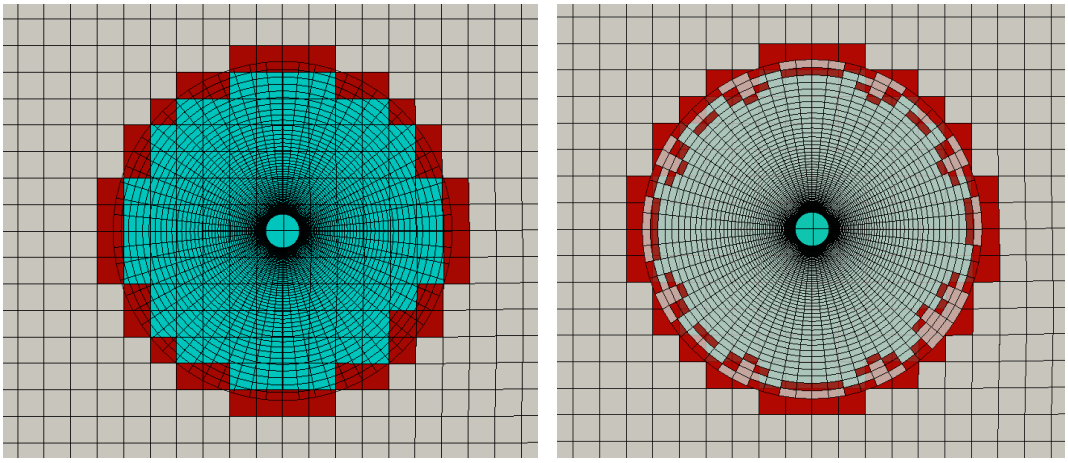

(a) (b)

Figure 11. Cylinder overset mesh close-up with fringe (red) and hole (blue) tagged cells.

The solution for the three case tests converged and their Mach field results can be seen in Fig. 12 comparing the P1Q1 single and overset meshes and in Fig. 13 for the high-order P4Q4 single mesh. The solution for low-order meshes are not

symmetrical as expected in both single and overset meshes, but the P4Q4 high-order mesh achieve the double symmetry once can handle a better geometric representation of cylinder.

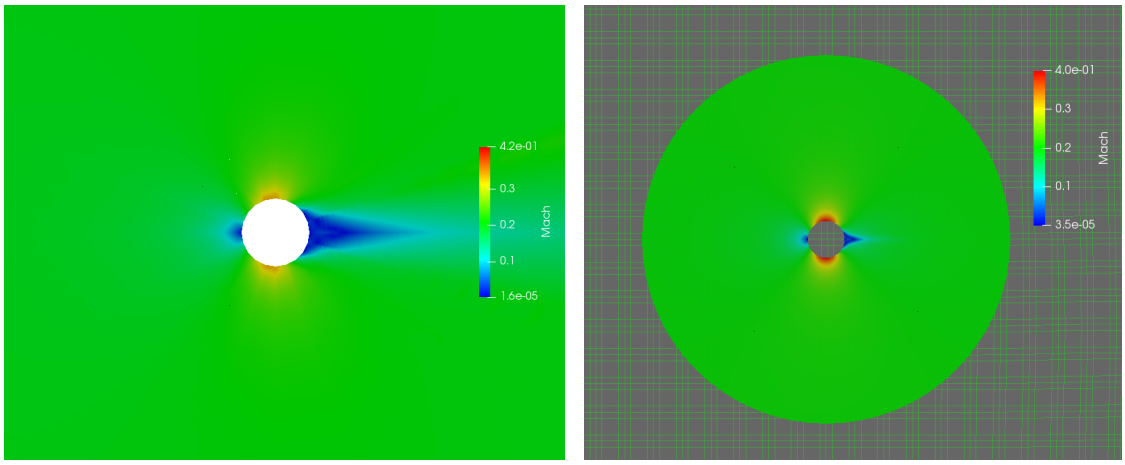

(a) Mach solution for cylinder single mesh, P1Q1. (b) Mach solution for cylinder overset mesh P1Q1.

Figure 12. Mach field solution.

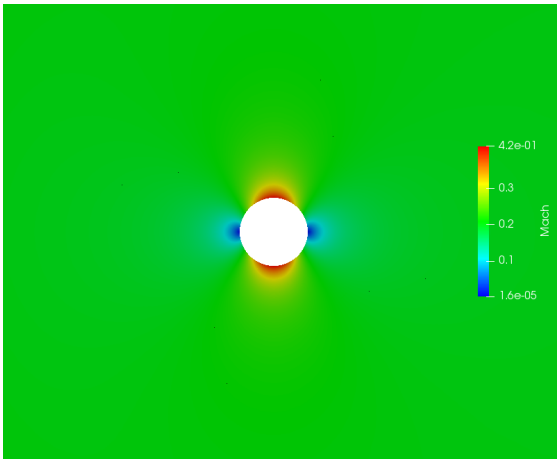

Figure 13. Mach solution for cylinder single mesh, P4Q4.

6 CONCLUDING REMARKS

The solver has been successfully validated through the tests for both low and high order achieving the expected results in the literature. The overset results obtained have demonstrated the capability of the kd-tree for the geometric searching problem as well as the face-based approach for the interpolation. The mesh generation for the overset cases is crucial in order to achieve the presented results once several edge cases can appear around the overset region in particular for high-order meshes where only a part of the fringe flux points at the same edge are inside a donor cell. Therefore, the flux can not be reconstructed for this scenario and future work extensions must be done to handle this problem properly adding robustness to the presented technique.

7 ACKNOWLEDGEMENTS

The authors gratefully acknowledge the support for the present research provided by Conselho Nacional de Desenvolvimento Científico e Tecnológico, CNPq, under the Research Grant No. 309985/2013-7. The present work is also supported by Fundação de Amparo à Pesquisa do Estado de São Paulo, FAPESP, under the Research Grant No. 2013/07375-0.

8 REFERENCES

Aguiar, A.R.B., 2018. *Study of Viscous Flows Using High-Order Methods and Curved Boundary Treatment*. Master's thesis, Graduate Program in Space Science and Technology, Instituto Tecnológico de Aeronáutica, São José dos Campos, Brasil.

Bentley, J.L., 1975. "Multidimensional binary search trees used for associative searching". *Communications of the ACM*, Vol. 18, No. 69, p. 509–517.

Crabill, J.A., Sitaraman, J. and Jameson, A., 2016. "A high-order overset method on moving and deforming grids". In *AIAA Modeling and Simulation Technologies Conference*. doi:10.2514/6.2016-3225. URL https://arc.aiaa.org/doi/abs/10.2514/6.2016-3225.

Duan, Z. and Wang, Z.J., 2020. "High-order overset flux reconstruction method for dynamic moving grids". *AIAA Journal*, Vol. 58, No. 10, pp. 4534–4547. doi:10.2514/1.J059185. URL https://doi.org/10.2514/1.J059185.

Duan, Z. and Wang, Z.J., 2017. "High order FR/CPR method for overset meshes". In *23rd AIAA Computational Fluid Dynamics Conference – AIAA Aviation Forum,* AIAA Paper No. 2017-3094. Denver, CO. doi:10.2514/6.2017-3094. URL https://arc.aiaa.org/doi/abs/10.2514/6.2017-3094.

Duan, Z. and Wang, Z.J., 2019. "A high order overset FR/CPR method for dynamic moving grids". doi:10.2514/6.2019-1399. URL https://arc.aiaa.org/doi/abs/10.2514/6.2019-1399.

Galbraith, M.C., 2013. *A Discontinuous Galerkin Chimera Overset Solver*. Ph.D. thesis, Doctor Program in Aerospace Engineering, University of Cincinnati, Cincinnati, OH.

Gottlieb, S., Grant, Z.J. and Isherwood, L., 2018. "Strong stability preserving integrating factor Runge-Kutta methods". *SIAM Journal on Numerical Analysis*, Vol. 56, No. 6, p. 3276–3307.

Liu, Y., Vinokur, M. and Wang, Z.J., 2006. "Spectral difference method for unstructured grids I: Basic formulation". *Journal of Computational Physics*, Vol. 216, pp. 780–801.

May, G. and Jameson, A., 2006. "A spectral difference method for the Euler and Navier-Stokes equations on unstructured meshes". In AIAA Paper No. 2006-0304, *Proceedings of the 44th AIAA Aerospace Sciences Meeting*. Reno, NV.

Moreira, F.M., 2016. *A Study of High-Order Unstructured Spectral Difference Schemes for Compressible Flows*. Master's thesis, Graduate Program in Space Science and Technology, Instituto Tecnológico de Aeronáutica, São José dos Campos, Brasil.

Roe, P., 1981. "Approximate riemann solvers, parameter vectors, and difference schemes". *Journal of Computational Physics*, Vol. 43, No. 2, p. 357–372.

Ruuth, S., Spiteri, R. and Ruuth, J., 2002. "A new class of optimal high-order strong-stability-preserving time discretization methods". *SIAM J. Numer. Anal.*, Vol. 40. doi:10.1137/S0036142901389025.

Shapiro, A.H., 1953. *The Dynamics and Thermodynamics of Compressible Fluid Flow*. Wiley, New York.

Skrodzki, M., 2019. "The k-d tree data structure and a proof for neighborhood computation in expected logarithmic time".

van den Abeele, K., 2009. *Development of High-Order Accurate Schemes for Unstructured Grids*. Ph.D. thesis, Doctor Program in Mechanical Engineering, Vrije Universiteit Brussel, Brussels, Belgium.

van den Abeele, K., Lacor, C. and Wang, Z.J., 2007. "On the connection between the spectral volume and spectral difference method". *Journal of Computational Physics*, Vol. 227, pp. 877–885.

Wang, Z.J., 2002. "Spectral (finite) volume method for conservation laws on unstructured grids: Basic formulation". *Journal of Computational Physics*, Vol. 178, No. 1, pp. 210–251.

Wang, Z.J., Cagnone, J.S., Careni, D., de Wiart, C.C., Couaillier, V., Fidkowski, C., Galbraith, M., Hartman, R., Gooch, C.O., Persson, P.O., Hillewaert, K., Ekaterinaris, J., Huynh, H.T., Kroll, N. and Vincent, P., 2015. "HiOCFD4 4th International Workshop on High-Order CFD Methods". https://how4.cenaero.be.

Wang, Z.J. and Liu, Y., 2002. "Spectral (finite) volume method for conservation laws on unstructured grids II: Extension to two-dimensional scalar equation". *Journal of Computational Physics*, Vol. 179, No. 2, pp. 665–698.

Wang, Z.J., Liu, Y., May, G. and Jameson, A., 2007. "Spectral difference method for unstructured grids II: Extension to the Euler equations". *Journal of Scientific Computing*, Vol. 32, No. 1, pp. 3938–3956.

9 RESPONSIBILITY NOTICE

The authors are solely responsible for the printed material included in this paper.